Available online at www.sciencedirect.com
SCIENCE DIRECT®
Acta Materialia 52 (2004) 1451–1467
Acta MATERIALIA
www.actamat-journals.com

# Atomistic modeling of the γ and γ′-phases of the Ni–Al system

Y. Mishin *

*School of Computational Sciences, George Mason University, 4400 University Drive, Fairfax, VA 220304444, USA*

Received 28 October 2003; received in revised form 28 October 2003; accepted 26 November 2003

**Abstract**

A new embedded-atom potential has been developed for $Ni_3Al$ by fitting to experimental and first-principles data. The potential describes lattice properties of $Ni_3Al$, point defects, planar faults, as well as the γ and γ′ fields on the Ni–Al phase diagram. The potential is applied to calculate the energies of coherent Ni/$Ni_3Al$ interphase boundaries with three different crystallographic orientations. Depending on the orientation, the interface energy varies between 12 and 46 mJ/m$^2$. Coherent γ/γ′ interfaces existing at high temperatures are shown to be more diffuse and are likely to have a lower energy than Ni/$Ni_3Al$ interfaces.


*Keywords:* Computer modeling; Interatomic potential; Intermetallic compounds; Planar faults; Phase diagram

## 1. Introduction

$Ni_3Al$ is a technologically important intermetallic compound known for exhibiting an increase in the yield strength with temperature over a temperature range (yield stress anomaly) [1]. This compound also forms the basis of the γ′-phase which strengthens commercial Ni-base superalloys by the precipitation hardening mechanism [2,3]. Small, usually cuboidal, precipitates of the γ′-phase embedded in Ni-base FCC solid solution (γ-phase) impose resistance to dislocation slip and increase the strength and creep resistance of superalloys. Atomistic computer simulations offer a means of gaining a better understanding of dislocation behavior in $Ni_3Al$ and in the γ/γ′ structure, see for example [4–8]. Point defects and diffusion in $Ni_3Al$ have also been examined by atomistic simulations [9–14]. Diffusion is an important factor in the high-temperature behavior of $Ni_3Al$ and superalloys, as are the interphase boundaries γ/γ′. Diffusion controls the degradation rate of the γ/γ′ structure at high temperatures and the dislocation processes accompanying creep. The structure and energy of γ/γ′ interfaces influence the slip transfer between the two phases and the thermodynamics stability of γ′ particles.

The credibility of results delivered by atomistic simulations largely depends on the robustness of interatomic potentials employed in the simulations. Most simulations employ many-body potentials based on the Finnis–Sinclair method [15] or the embedded-atom method (EAM) [16]. Several EAM potentials have been proposed for $Ni_3Al$ (see [17] for a review), the best known of them being the potentials by Foiles and Daw (FD) [9] and by Voter and Chen (VC) [18]. All $Ni_3Al$ potentials developed so far have been fit to *experimental* values of the lattice parameter, cohesive energy, elastic constants and other experimental properties.

It has recently been recognized that the incorporation of *first-principles* data in the fitting database, together with experimental data, can significantly improve the reliability of interatomic potentials [19–26]. First-principles data sample a larger area of configuration space than experimental data do, including configurations far away from equilibrium states. This broader sampling improves the transferability of potentials to various local environments that can be encountered during atomistic simulations. Even if the accuracy of fit to particular experimental numbers remains the same, potentials developed by this scheme tend to be more robust. This scheme has recently been applied to construct an accurate EAM potential for the B2–NiAl compound of the Ni–Al system [24]. Unfortunately, properties of Ni and $Ni_3Al$ predicted by that potential are not at a

* Tel.: +1-703-993-3984; fax: +1-703-993-1993.
*E-mail address:* ymishin@gmu.edu (Y. Mishin).

1359-6454/$30.00 
doi:10.1016/j.actamat.2003.11.026

level of accuracy that would warrant its application to atomistic simulations of these phases.

Therefore, in this work we shift the focus to Ni and $Ni_3Al$. We will apply our scheme [20,23,24,26] to construct an accurate EAM potential describing Ni, $Ni_3Al$, as well as the thermodynamic equilibrium between the $\gamma$ and $\gamma'$-phases of the Ni–Al system. We are testing the new potential by calculating a large variety of properties ranging from phonon frequencies and thermal expansion to the Ni–Al phase diagram and $\gamma/\gamma'$ interfaces. Such a detailed characterization of a potential is essential for its future applications. We also discuss the issue of global transferability (or rather, lack thereof) of existing EAM potentials across the entire Ni–Al phase diagram.

## 2. Construction of the potentials

The EAM represents the total energy $E_{\rm tot}$ of a collection of atoms in the form [16]

$$E_{\rm tot} = \frac{1}{2}\sum_{i,j}\Phi_{ij}(r_{ij}) + \sum_i F_i(\overline{\rho}_i). \tag{1}$$

Here $\Phi_{ij}(r_{ij})$ is the pair-interaction energy between atoms $i$ and $j$ separated by a distance $r_{ij}$, $F_i$ is the embedding energy of atom $i$ and $\overline{\rho}_i$ is the host electron density induced by all surrounding atoms $j$ at the location of atom $i$. The host electron density is given by

$$\overline{\rho}_i = \sum_{j\neq i}\rho_j(r_{ij}), \tag{2}$$

where $\rho_j(r)$ is the electron-density function assigned to atom $j$. The pair-interaction, electron-density and embedding functions depend on the chemical sorts of atoms. Therefore, a full description of a binary system A–B requires seven potential functions: $\Phi_{\rm AA}(r)$, $\Phi_{\rm AB}(r)$, $\Phi_{\rm BB}(r)$, $\rho_{\rm A}(r)$, $\rho_{\rm B}(r)$, $F_{\rm A}(\overline{\rho})$ and $F_{\rm B}(\overline{\rho})$. All functions but $\Phi_{\rm AB}(r)$ can be obtained by fitting to properties of individual elements A and B. The cross-interaction function $\Phi_{\rm AB}(r)$ can be then fitted to properties of binary alloys and/or compounds of the system. While implementing this fit, we take advantage of certain mathematical transformations that do not affect the total energies of elements A and B but do change the energy of the binary system. Such transformations include

$$\rho_{\rm B}(r) \to s_{\rm B}\rho_{\rm B}(r), \tag{3}$$

$$F_{\rm B}(\overline{\rho}) \to F_{\rm B}(\overline{\rho}/s_{\rm B}), \tag{4}$$

$$F_{\rm A}(\overline{\rho}) \to F_{\rm A}(\overline{\rho}) + g_{\rm A}\overline{\rho}, \tag{5}$$

$$F_{\rm B}(\overline{\rho}) \to F_{\rm B}(\overline{\rho}) + g_{\rm B}\overline{\rho}, \tag{6}$$

$$\Phi_{\rm AA}(r) \to \Phi_{\rm AA}(r) - 2g_{\rm A}\rho_{\rm A}(r), \tag{7}$$

$$\Phi_{\rm BB}(r) \to \Phi_{\rm BB}(r) - 2g_{\rm B}\rho_{\rm B}(r). \tag{8}$$

The transformation coefficients $s_{\rm B}$, $g_{\rm A}$ and $g_{\rm B}$ can be used as additional adjustable parameters when fitting the cross-interaction function [18].

Following this scheme, for the Ni–Al system we first need to create EAM potentials for pure Ni and Al and then construct a cross-interaction potential $\Phi_{\rm NiAl}(r)$. For Al, we will reuse the EAM potential developed in our recent work [26] as a part of the Ti–Al potential set. We will reproduce here the optimized fitting parameters and the relevant properties of Al to make this paper self-contained. For Ni, we will develop a new potential following exactly the same fitting procedure as for Al.

For both Ni and Al, the electron density is postulated in the form

$$\rho(r) = \psi\left(\frac{r-r_{\rm c}}{h}\right)[A_0 z^y {\rm e}^{-\gamma z}(1 + B_0{\rm e}^{-\gamma z}) + C_0], \tag{9}$$

where $z = r - r_0$ and $\psi(x)$ is a cutoff function defined as

$$\psi(x) = \frac{x^4}{1+x^4}, \tag{10}$$

if $x < 0$ and 0 if $x \geqslant 0$. Eq. (9) parameterizes $\rho(r)$ with eight fitting parameters: $A_0$, $B_0$, $C_0$, $r_0$, $r_{\rm c}$, $h$, $y$ and $\gamma$. One of them is eliminated by imposing the condition of unit host electron density in the equilibrium FCC lattice. The pair-interaction function is parameterized in a generalized Lennard–Jones form

$$\Phi(r) = \psi\left(\frac{r-r_{\rm c}}{h}\right)\left[\frac{V_0}{b_2-b_1}\left(\frac{b_2}{z^{b_1}} - \frac{b_1}{z^{b_2}}\right) + \delta\right], \tag{11}$$

where $z = r/r_1$. The fitting parameters are $b_1$, $b_2$, $r_1$, $V_0$ and $\delta$. Notice that the cutoff function guarantees that both functions $\rho(r)$ and $\Phi(r)$ and their derivatives up to the second one turn smoothly to zero at the common cutoff distance $r_{\rm c}$.

The embedding energy $F(\overline{\rho})$ is obtained by inverting the universal equation of state [26,27] of the FCC structure. The latter is postulated in the form

$$E(a) = E_0\left[1 + \alpha x + \beta\alpha^3 x^3\frac{2x+3}{(x+1)^2}\right]{\rm e}^{-\alpha x}, \tag{12}$$

where $x = a/a_0 - 1$ and

$$\alpha = \left(-\frac{9\Omega_0 B}{E_0}\right)^{1/2}.$$

In these equations, $E$ is the crystal energy per atom relative to a set of isolated atoms, $E_0$ is the cohesive energy (minimum of $E$), $a$ is the lattice parameter, $a_0$ is the equilibrium value of $a$, $\Omega_0 = a_0^3/4$ is the equilibrium atomic volume, $B$ is the bulk modulus and $\beta$ is an adjustable parameter.

This procedure guarantees an exact fit to the equilibrium lattice parameter, cohesive energy and bulk modulus. The cubic term in Eq. (12) allows us to vary the crystal energy under strong compressions without altering $E_0$, $a_0$ or $B$. This gives us an extra degree of

freedom to achieve a more accurate match to the experimental pressure–volume relation by adjusting the parameter $\beta$. This parameterization describes an elemental solid with 13 fitting parameters.

For the cross-interaction function $\Phi_{NiAl}(r)$ we also use the generalized Lennard–Jones form, Eq. (11), with seven fitting parameters $b_1$, $b_2$, $V_0$, $\delta$, $r_1$, $r_c$ and $h$. Together with the transformation coefficients, the binary system is described by the total of 36 parameters. This is more than was used in previous potentials for $Ni_3Al$ [9,17,18], but the increased number of parameters is well justified by the much larger fitting database employed in this work.

For Ni and Al, the fitting database includes the experimental values of the lattice parameters, cohesive energies, elastic constants $c_{ij}$, and the vacancy formation energy $E_v^f$ and migration energy $E_v^m$. Thermal expansion factors at several temperatures are also included with a small weight. The first-principles data are used in the form of energy–volume relations for several structures: FCC, HCP, BCC, simple cubic (SC), $L1_2$ and diamond. Here, the $L1_2$ structure is a defected FCC lattice with one unrelaxed vacancy per cubic unit cell. The first-principles energies were calculated by the linearized augmented plane-wave (LAPW) method [28] within the local density approximation (LDA) [29]. The Al calculations were also performed within the generalized gradient approximation and the results were found to be similar to the LDA calculations [26]. Before the fitting process, interatomic distances in all structures are scaled by the same factor so that to make the FCC lattice parameter match the experimental value [20,23,24,26]. This scaling is intended to correct for the fact that LDA tends to slightly compress all distances. Because of the different reference energies in the EAM and first-principles calculations, it is relative, rather then absolute, structural energies that were used in the fit. For the cross-interaction function, the fitting database includes the experimental values of the lattice parameter and elastic constants of the $L1_2$ structure of $Ni_3Al$. The first-principles data contain the formation energy versus volume relations for the following ordered structures: $L1_2$–$Ni_3Al$, $D0_{22}$–$Ni_3Al$, $D0_3$–$Ni_3Al$, B1–NiAl, B2–NiAl, $L1_0$–NiAl, $L1_1$–NiAl, B32–NiAl and 40–NiAl (NbP prototype). Between 10 and 20 volumes around the equilibrium were computed for each structure. Notice that these data include only two stoichiometries: $Ni_3Al$ and NiAl. Again, all interatomic distances are scaled by the same factor so that to match the experimental lattice parameter of $Ni_3Al$. All first-principles data used here were calculated in our previous work [20,24,26].

The potential functions were optimized by minimizing the weighted mean-squared deviation of properties from their target values by the simulated annealing method. The optimized fitting parameters are listed in Table 1. The potential functions are available in a tabulated format through the World Wide Web at http://cst-www.nrl.navy.mil/bind/eam. As an illustration, Fig. 1 shows the pair-interaction functions transformed to the effective pair format [24,26,30].

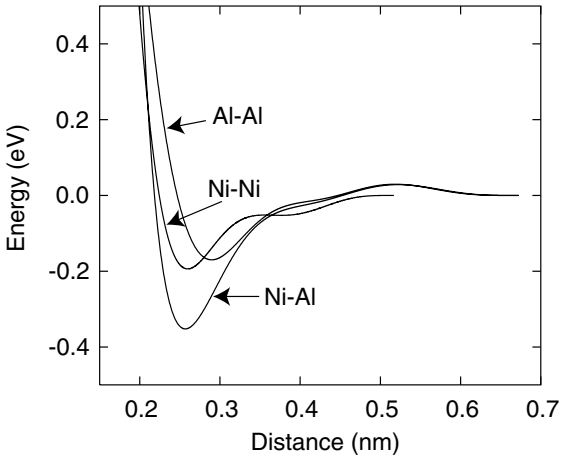


Fig. 1. Pair-interaction functions of the EAM potential in the effective pair format.

Table 1
Optimized values of fitting parameters of the EAM potentials for Ni, Al and $Ni_3Al$

| Al | | Ni | | $Ni_3Al$ | |
|---|---|---|---|---|---|
| Parameter | Value | Parameter | Value | Parameter | Value |
| $r_c$ (nm) | 0.6725 | $r_c$ (nm) | 0.5168 | $r_c$ (nm) | 0.6500 |
| $h_c$ (nm) | 0.3294 | $h_c$ (nm) | 0.3323 | $h_c$ (nm) | 0.2658 |
| $V_0$ (eV) | $-3.5032 \times 10^3$ | $V_0$ (eV) | $-3.5126 \times 10^3$ | $V_0$ (eV) | 0.6068 |
| $r_1$ (nm) | 0.2858 | $r_1$ (nm) | $3.8673 \times 10^{-5}$ | $r_1$ (nm) | 0.4834 |
| $b_1$ | $8.5951 \times 10^{-2}$ | $b_1$ | $4.7067 \times 10^{-3}$ | $b_1$ | 2.9013 |
| $b_2$ | $5.0124 \times 10^{-2}$ | $b_2$ | 0.15106 | $b_2$ | 1.0001 |
| $\delta$ (eV) | $3.7503 \times 10^3$ | $\delta$ (eV) | $3.6046 \times 10^3$ | $\delta$ (eV) | −3.4108 |
| $y$ | $2.0080 \times 10^1$ | $y$ | $1.9251 \times 10^1$ | $s_{Al}$ | 0.9549 |
| $\gamma$ (1/nm) | $4.2799 \times 10^1$ | $\gamma$ (1/nm) | $1.6802 \times 10^3$ | $g_{Ni}$ (eV) | $5.8549 \times 10^1$ |
| $B_0$ (nm) | $1.1927 \times 10^4$ | $B_0$ (nm) | $1.1914 \times 10^4$ | $g_{Al}$ (eV) | $-1.8162 \times 10^1$ |
| $C_0$ (1/nm$^3$) | $8.6029 \times 10^1$ | $C_0$ (1/nm$^3$) | $2.0329 \times 10^2$ | | |
| $r_0$ (nm) | $5.2755 \times 10^{-2}$ | $r_0$ (nm) | −0.3138 | | |
| $\beta$ | $0.4890 \times 10^{-2}$ | $\beta$ | $0.4890 \times 10^{-2}$ | | |

## 3. Properties of Ni and Al

Table 2 summarizes lattice properties of Ni and Al calculated with the present EAM potentials in comparison with experimental data [31–34]. The table includes the phonon frequencies at the zone-boundary points $X$, $L$ and $K$, but the calculations were actually performed all across the Brillouin zone. While the elastic constants are fit to experiment very accurately, the phonon frequencies (which were not included in the fit) tend to overestimate the experimental values in the high-frequency range. For Al, the optimized value of the pressure parameter $\beta$ [see Eq. (12)] provides an excellent agreement with the experimental pressure–volume relation up to 700 GPa [26]. Because equally reliable high-pressure data for Ni are not available, we chose the same $\beta$ value as for Al. Thermal expansion factors of Ni and Al were computed by the Monte Carlo method in which atoms were allowed to move around their lattice positions and the volume could fluctuate to ensure the zero-pressure condition (NPT ensemble) [35,36]. A 864-atom supercell was used in these calculations. The agreement with experiment [37] is reasonable (Fig. 2). Even though a few thermal expansion factors were included in the fit, the potentials

Table 2
Lattice properties of Ni and Al calculated with the present EAM potentials in comparison with experimental data

| Property | Ni | | Al | |
|---|---|---|---|---|
| | Experiment | EAM | Experiment | EAM |
| $a_0$ (nm)[a] | 0.352[b] | 0.352 | 0.405[c] | 0.405 |
| $E_0$ (eV)[a] | −4.45[b] | −4.45 | −3.36[c] | −3.36 |
| *Elastic constants (GPa):*[a] | | | | |
| $B$ | 181.0[d] | 181.0 | 79.0[d] | 79.0 |
| $c_{11}$ | 246.5[d] | 241.3 | 114.0[d] | 116.8 |
| $c_{12}$ | 147.3[d] | 150.8 | 61.9[d] | 60.1 |
| $c_{44}$ | 124.7[d] | 127.3 | 31.6[d] | 31.7 |
| *Phonon frequencies (THz):* | | | | |
| $L(X)$ | 8.55[e] | 9.90 | 9.69[e] | 10.1 |
| $T(X)$ | 6.27[e] | 6.78 | 5.80[e] | 6.08 |
| $L(L)$ | 8.88[e] | 9.80 | 9.69[e] | 9.90 |
| $T(L)$ | 4.24[e] | 4.29 | 4.19[e] | 3.98 |
| $L(K)$ | 7.30[e] | 7.81 | 7.59[e] | 8.20 |
| $T_1(K)$ | 5.78[e] | 5.98 | 5.64[e] | 5.58 |
| $T_2(K)$ | 7.39[e] | 9.02 | 8.65[e] | 9.27 |

[a] Included in the fitting database.
[b] Ref. [31].
[c] Ref. [32].
[d] Ref. [33].
[e] Ref. [34].

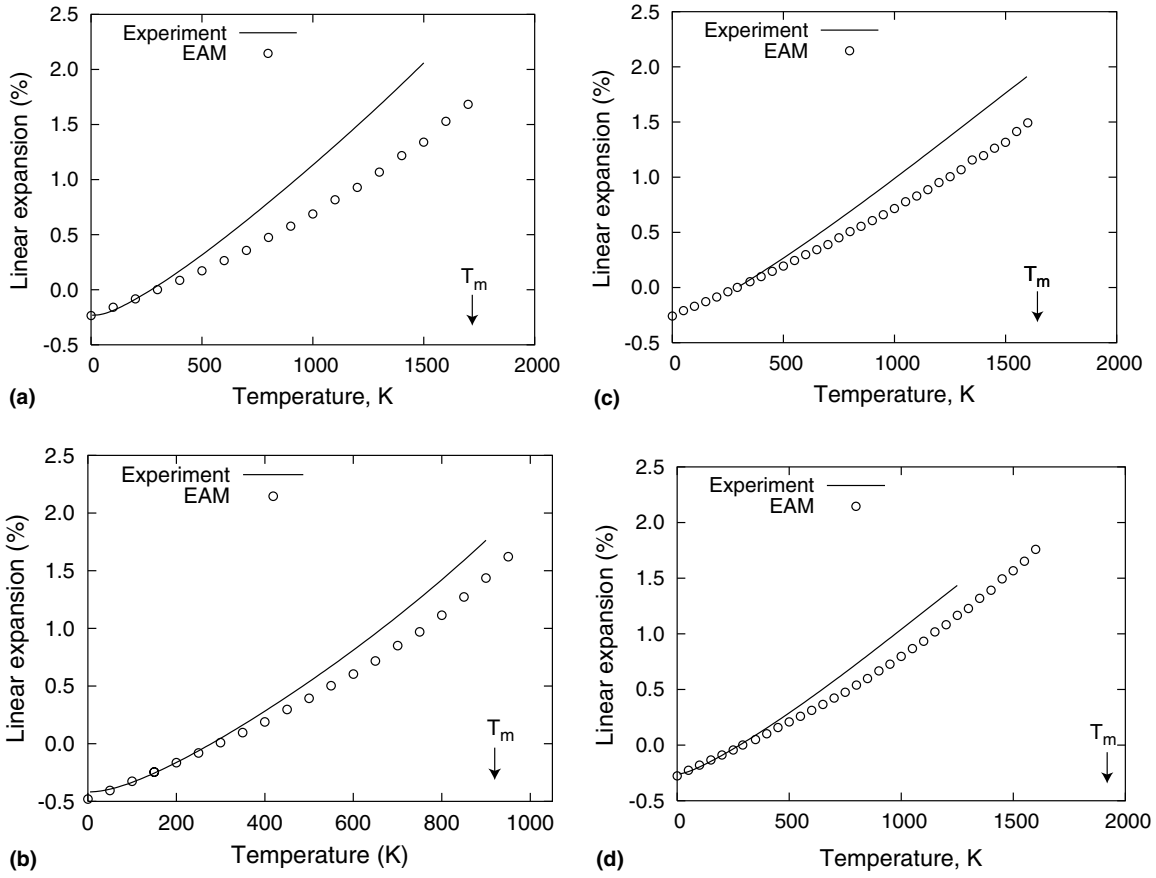


Fig. 2. Linear thermal expansion of (a) Ni, (b) Al, (c) $Ni_3Al$ and (d) NiAl relative to room temperature (293 K). The EAM calculations employed the NPT Monte Carlo method. The experimental data are the 'recommended' values from [37]. The arrow marks the experimental melting point $T_m$.

underestimate the expansion at high temperatures. Most of this discrepancy arises from the fact that thermal expansion was treated during the fitting process in the local harmonic approximation. The subsequent more accurate Monte Carlo simulations gave smaller expansion factors.

Lattice defect energies in Ni and Al calculated with the EAM potentials are compared with experimental data [38–41] in Table 3. All defect energies were obtained by fully relaxed calculations. The vacancy formation and migration energies were included in the fit, but all other energies are predictions of the potentials. The fact that the vacancy properties are in a good agreement with experiment makes these potentials suitable for diffusion simulations. The planar fault energies (intrinsic stacking fault $\gamma_{SF}$ and symmetrical twin boundary $\gamma_T$) also compare with experiment reasonably well. For Al, $\gamma_{SF} = 115$ mJ/m$^2$ lies on the lower side of the accepted experimental value (166 mJ/m$^2$) and the results of first-principles calculations [42,43]. Reliable experimental data for $\gamma_{us}$ (unstable stacking fault energy) are not available. The surface energies are quite reasonable for Ni but less accurate for Al.

The equilibrium structural energies relative to the FCC structure (Table 4) compare with first-principles calculations fairly well. It should be noted that it was the energy–volume curves that were used in the fit and not the equilibrium energies. In agreement with first-principles calculations [20], the BCC and SC structures of both metals are mechanically unstable.

Although the motivation for constructing the Ni and Al potentials was to obtain supporting functions for $Ni_3Al$, both potentials turn out to be accurate enough to be used separately in atomistic simulations of these metals. They have advantages over some of the existing EAM potentials, particularly with respect to the stacking fault energies, vacancy characteristics, thermal expansion and high-pressure behavior. The potentials are based on simple analytical functions and should give stable results in quasi-harmonic calculations as well as in molecular dynamics and Monte Carlo simulations at high temperatures.

Table 3
Lattice defect energies in Ni and Al calculated with the present EAM potentials in comparison with experimental data

| Property | Ni | | Al | |
|---|---|---|---|---|
| | Experiment | EAM | Experiment | EAM |
| *Vacancy (eV):*[a] | | | | |
| $E_v^f$ | 1.60[b] | 1.57 | 0.68[c] | 0.71 |
| $E_v^m$ | 1.30[d] | 1.19 | 0.65[c] | 0.65 |
| *Planar faults (mJ/m$^2$):* | | | | |
| $\gamma_{SF}$ | 125[e] | 134 | 166[e] | 115 |
| $\gamma_{us}$ | | 298 | | 151 |
| $\gamma_T$ | 43[e] | 68 | 75[e] | 63 |
| *Surfaces (mJ/m$^2$):* | | | | |
| (1 1 0) | 2280[f] | 2087 | 980[f] | 792 |
| (1 0 0) | 2280[f] | 1936 | 980[f] | 607 |
| (1 1 1) | 2280[f] | 1759 | 980[f] | 601 |

[a] Included in the fitting database.
[b] Ref. [38].
[c] Ref. [39].
[d] Ref. [40].
[e] Ref. [41].
[f] For average orientation, Ref. [41].

Table 4
Equilibrium energies (in eV) of alternative structures of Ni and Al obtained with the present EAM potential in comparison with first-principles LAPW calculations [20,24,26]

| | Ni | | Al | |
|---|---|---|---|---|
| Structure | LAPW | EAM | LAPW | EAM |
| HCP | 0.03 | 0.02 | 0.04 | 0.03 |
| BCC | 0.11 | 0.07 | 0.09 | 0.09 |
| $L1_2$ | 0.66 | 0.54 | 0.27 | 0.33 |
| SC | 1.00 | 0.72 | 0.36 | 0.30 |
| Diamond | 1.94 | 1.42 | 0.75 | 0.88 |

The energies are given relative to the equilibrium FCC structure.

## 4. Lattice properties and structural stability of $Ni_3Al$

The lattice parameter and elastic constants of $Ni_3Al$ are accurately fit to the experimental values [4,44] (Table 5). The cohesive energy $E_0$ is also quite close to the experimental value −4.62 eV [4,44]. The cohesive energy was not used in the fit directly but was involved indirectly through the first-principles formation energy of $Ni_3Al$ and the experimental cohesive energies of Ni and Al.

The phonon dispersion curves in $Ni_3Al$ calculated with the new potential generally agree with experimental curves measured by neutron scattering at room temperature [45]. Table 6 compares the calculated and experimental phonon frequencies at the zone center $\Gamma$ and the zone boundary points $X$, $R$ and $M$. The table reveals, however, that the potential tends to overestimate phonon frequencies, especially in the high-frequency range. This discrepancy mainly reflects the disagreement between two existing sets of experimental data. Indeed, the elastic constants deduced from the phonon dispersion data are $c_{11} = 212$, $c_{12} = 125$ and $c_{12} = 106$ GPa [45]. On the other hand, we fitted the potential to higher values of the elastic constants (see Table 5) which had been obtained by Yoo [4,44] by an extrapolation of room-temperature

Table 5
Lattice properties of $Ni_3Al$ calculated with the present EAM potential in comparison with experimental data

| | | | Elastic constants (GPa)[a] | | |
|---|---|---|---|---|---|
| | $a_0$ (nm)[a] | $E_0$ (eV) | $c_{11}$ | $c_{12}$ | $c_{44}$ |
| Experiment[b] | 0.357 | −4.620 | 230 | 149 | 132 |
| EAM | 0.3571 | −4.626 | 236 | 154 | 127 |

[a] Included in the fitting database.
[b] Refs. [4,44].

Table 6
Phonon frequencies (in THz) of $Ni_3Al$ calculated with the present EAM potential in comparison with experimental data [45]

| Point | Branch | Exp. | EAM |
|---|---|---|---|
| $\Gamma = [0\,0\,0]$ | $O_1$ | 6.12 | 6.68 |
| | $O_2$ | 6.83 | 7.68 |
| | $O_3$ | 9.85 | 12.21 |
| $X = \frac{1}{2}[0\,0\,1]$ | LA | 6.11 | 6.43 |
| | TA | 4.59 | 4.83 |
| | $LO_1$ | 5.82 | 6.57 |
| | $TO_1$ | 5.22 | 5.47 |
| | $LO_2$ | 6.59 | 6.73 |
| | $TO_2$ | 7.29 | 8.13 |
| | $LO_3$ | 9.45 | 9.79 |
| | $TO_3$ | 9.68 | 11.46 |
| $R = \frac{1}{2}[1\,1\,1]$ | LA | 5.77 | 5.24 |
| | TA | 4.10 | 4.35 |
| | $LO_1$ | 4.48 | 4.64 |
| | $TO_1$ | 4.30 | 4.64 |
| | $LO_2$ | 8.85 | 9.38 |
| | $TO_2$ | 5.77 | 5.24 |
| | $LO_3$ | 10.20 | 12.16 |
| | $TO_3$ | 10.20 | 12.16 |
| $M = \frac{1}{2}[0\,1\,1]$ | LA | 4.70 | 4.75 |
| | $T_1A$ | 5.70 | 6.55 |
| | $T_2A$ | 3.98 | 4.37 |
| | $LO_1$ | 7.55 | 8.02 |
| | $T_1O_1$ | 5.62 | 6.75 |
| | $T_2O_1$ | 4.48 | 4.66 |
| | $LO_2$ | 7.55 | 8.19 |
| | $T_1O_2$ | 5.62 | 6.75 |
| | $T_2O_2$ | 4.70 | 4.75 |
| | $LO_3$ | 9.80 | 10.98 |
| | $T_1O_3$ | 8.82 | 10.43 |
| | $T_2O_3$ | 9.70 | 10.98 |

Branch labeling: O, optical; A, acoustical; L, longitudinal; T, transversal.

Table 7
Formation energies of alternative structures of $Ni_3Al$ and NiAl obtained with the present EAM potential

| Structure | EAM | LAPW |
|---|---|---|
| $Ni_3Al$: | | |
| $L1_2$ | −0.4486 | −0.4680 |
| $D0_{23}$ | −0.4401 | |
| $D0_{19}$ | −0.4392 | |
| $D0_3$ | −0.4356 | −0.4093 |
| $D0_{22}$ | −0.4318 | −0.4305 |
| $D0_{11}$ | −0.0147 | |
| NiAl: | | |
| B2 | −0.5918 | −0.7041 |
| $L1_0$ | −0.5139 | −0.5469 |
| "40" | −0.4762 | −0.5435 |
| B32 | −0.4721 | −0.3544 |
| B20 | −0.4283 | |
| $L1_1$ | −0.3590 | −0.3251 |
| B1 | 0.0596 | −0.0335 |

The results of first-principles LAPW calculations [20,24] are included for comparison.

ultrasonic measurements [46] to 0 K. The larger elastic constants make the lattice stiffer and inevitably lead to an overall increase in phonon frequencies.

Thermal expansion coefficients of $Ni_3Al$ calculated by the NPT Monte Carlo method show a good agreement with experiment (Fig. 2(c)). Thermal expansion of $Ni_3Al$ was not used in the potential fit.

Table 7 summarizes the equilibrium formation energies of several structures of $Ni_3Al$ relative to FCC Ni and Al. For the structures used in the fit, the respective first-principles energies are also included. Notice that some of the structures, most notably $D0_{23}$ and $D0_{19}$, strongly compete with $L1_2$ for stability and have only slightly higher energies. These subtle energy differences between the structures are very important as they correlate with some of the planar fault energies in $Ni_3Al$ (see below).

## 5. Planar faults in $Ni_3Al$

Energies of planar faults in $Ni_3Al$ have a strong impact on the dislocation core structure and ultimately the deformation behavior of the material. The most common dislocations in $Ni_3Al$ are $\langle 1\,1\,0\rangle$ screw superdislocations dissociated into $1/2\langle 1\,1\,0\rangle$ superpartials separated by an antiphase boundary (APB) on a $\{1\,1\,1\}$ plane [1,7,47,48]. Each superpartial, in turn, can dissociate into Shockley partials separated by a complex stacking fault (CSF). An alternative, although less common scenario, is the dissociation of a superdislocation into $1/3\langle 2\,1\,1\rangle$ Kear superpartials bounding a superlattice intrinsic stacking fault (SISF). Thus, the (1 1 1) APB, CSF and SISF planar faults largely determine the dislocation core structure and mobility. Furthermore, at high temperatures the leading superpartial gliding on a $\{1\,1\,1\}$ plane, or its segments, can cross-slip into cubic $\langle 1\,0\,0\rangle$ planes and form locked configurations. The driving forces for this cross-slip are the elastic anisotropy creating a torque force between the two superpartials [49], as well as the APB anisotropy, with the (1 0 0) APB having a lower energy than the (1 1 1) APB. Because the cross-slip requires a constriction of the CSF, it is a thermally activated process which is considered to be responsible for the yield stress anomaly in $Ni_3Al$ [1,7,47,48].

Each planar fault is produced by a relative shift of two half-crystals by an appropriate translation vector parallel to the (1 1 1) (respectively, (1 0 0)) plane. To calculate the fault energy, first the so-called $\gamma$ surface [50] is computed for the (1 1 1) and (1 0 0) planes. The $\gamma$ surface represents a plot of the partially relaxed fault energy as a function of the translation vector. The partial relaxation allows only atomic displacements normal to the fault plane while in-plane displacements are prohibited. Local minima on the $\gamma$ surface represent stable planar faults. At the second step, the structures

corresponding to the minima are fully relaxed by allowing arbitrary atomic movements. The energy decrease at the second step is usually small (a few mJ/m$^2$).

All four types of fault in $Ni_3Al$ were found to be stable. In agreement with previous calculations [51,52], the equilibrium translation vectors of the (1 1 1) APB and CSF were found to be slightly shifted away from their ideal positions expected from hard-sphere considerations. In contrast, the positions of the SISF and (1 0 0) APB coincide with those dictated by symmetry. Table 8 reports the obtained fault energies and compares them with experimental data [53–55] and recent first-principles calculations [51,52,56,57]. The agreement with first-principles data is quite satisfactory. The lower APB energy on cubic planes relative to octahedral planes provides the required driving force for the cross-slip process.

Table 8 also contains the fault energies calculated with the FD [9,44] and VC [18,58] potentials. Their agreement with first-principles calculations appears to be less accurate. The FD potential strongly underestimates the (1 0 0) APB energy while the VC potential underestimates the CSF and especially SISF energies. It should be noted that the VC potential was fit to experimental energies of some of the faults, whereas the FD potential was not fit to any fault energies. Since our potential was not fit to planar fault energies either, we believe that its agreement with first-principles fault energies is due to the presence of first-principles structural energies in the fitting database. Indeed, the (1 0 0) APB energy is known to correlate with the energy difference between the $L1_2$ and $D0_{22}$ structures [51], both of which were included in the fit. Likewise, the SISF energy correlates with the $L1_2$–$D0_{19}$ energy difference. Although the $D0_{19}$ structure was not used in the fit, its energy is likely to be accurate due to the broad sampling of configuration space by other structures.

Table 8 demonstrates that there is a good agreement between experimental and first-principles energies for all faults except for SISF. In the latter case, the discrepancy is as large as on order of magnitude. One possible explanation for this discrepancy could conceivably be a decrease in the fault energies with temperature relative to their zero-temperature values. Notice that all calculated energies in Table 8 refer to 0 K. At finite temperatures, a fault can develop local deviations of the site occupation from the one in the ideal fault structure, which can reduce the excess free energy of the fault. One can speculate that this effect could be strongest for the SISF fault, which would then explain the above discrepancy.

In order to test this hypothesis, we have performed grand-canonical Monte Carlo calculations of equilibrium site occupation across each fault in stoichiometric $Ni_3Al$ at the temperature of $T = 1000$ K. Technical details of this method will be discussed later (Section 7). Fig. 3 shows the concentration of Ni atoms on Al sites (i.e., sites occupied by Al atoms at 0 K) as a function of

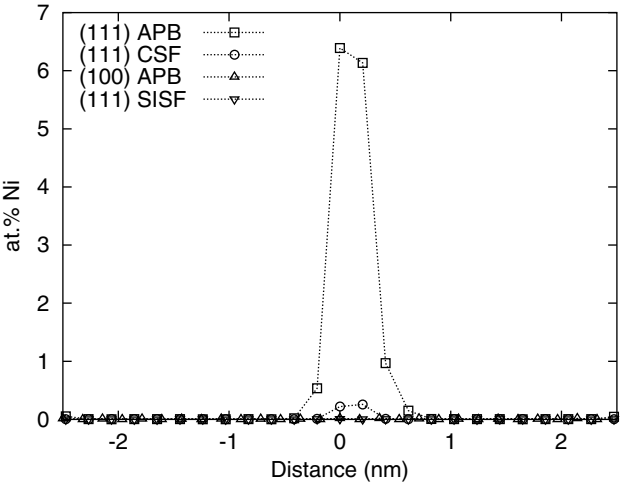


Fig. 3. Calculated Ni concentration on Al sites as a function of distance to the fault plane in stoichiometric $Ni_3Al$ at 1000 K. Obtained by grand-canonical Monte Carlo simulations.

Table 8
Comparison of calculated and experimental values of planar fault energies (in mJ/m$^2$) in $Ni_3Al$

| Fault | Experiment | Ab initio | EAM | | |
|---|---|---|---|---|---|
| | | | Present work | Refs. [9,44] | Refs. [18,58] |
| (1 1 1) APB | 180;[a] 175;[b] 195[c] | 188;[d] 210;[e] 172[f] | 252 | 156 | 142 |
| (1 1 1) CSF | 206;[a] 235;[b] 236[c] | 225;[e] 223[f] | 202 | 259 | 121[h] |
| (1 1 1) SISF | 6[b] | 80;[e] 79[f] | 51 | 96 | 13 |
| (1 0 0) APB | 104;[b] 160[c] | 121[g] | 80 | 28 | 83 |

[a] Ref. [53].
[b] Ref. [54].
[c] Ref. [55].
[d] Ref. [51].
[e] Ref. [52].
[f] Ref. [56].
[g] Ref. [57].
[h] Calculated in this work.

distance across the faults. The (1 1 1) APB shows significant deviations from the ideal site occupation, suggesting that its excess free energy may decrease with temperature. A quantification of this decrease is beyond the scope of this work. Qualitatively, however, this effect would bring our EAM-calculated (1 1 1) APB energy to a better agreement with experiment (cf. Table 8). For the CSF fault, the local antisite disorder is much weaker, whereas for the (1 0 0) APB and SISF it is negligible. Accordingly, the energies of these faults are not expected to change with temperature significantly.

These observations are in line with the calculations by Skinner et al. [59] who applied a thermodynamic integration method along an alchemy path in conjunction with molecular dynamics to evaluate the temperature dependencies of the (1 1 1) and (1 0 0) APB energies. They used a Finnis–Sinclair potential for $Ni_3Al$ constructed by Vitek et al. [6]. According to their calculation, the (1 1 1) APB energy decreases from 226 mJ/m$^2$ at 0 K to $193 \pm 31$ mJ/m$^2$ at 900 K. The (1 0 0) APB energy changes by a lesser amount, from 53 mJ/m$^2$ at 0 K to $44 \pm 57$ mJ/m$^2$ at 900 K [59].

Thus, contrary to our assumption, the SISF energy is unlikely to decrease with temperature significantly. This leaves the existing discrepancy between the first-principles and experimental SISF energies an open question that calls for a clarification in the future. Experimental fault energies are calculated from measured dislocation dissociation widths using elasticity theory. It cannot be excluded that the widely dissociated SISF dislocations observed in experiment [54,48] might not have been in true equilibrium.

The fact that the (1 1 1) APB and CSF faults are prone to local antisite disorder while the (1 0 0) APB and SISF are not is understandable from simple geometric considerations. Al atoms, which are separated from each other in the ideal $L1_2$ structure, become nearest neighbors across the (1 1 1) APB and CSF. Because of the large ordering energy of $Ni_3Al$ the existence of such neighbors is highly unfavorable and leads to relatively large fault energies (Table 8). When atoms become movable at high temperatures, some of the Al atoms involved in Al–Al bonds tend to be replaced by Ni atoms since this can decrease the configurational energy. In contrast, the first-neighbor environments at the (1 0 0) APB and SISF faults are similar to those in $L1_2$ structure. These faults can be thought of as layers of a slightly different crystal structure with the same stoichiometry. Their energy is, therefore, relatively low and the antisite disorder (if any) is not much different from that in the bulk. To reflect the physically different origin of the fault energy, Paxton and Sun [51] called the (1 1 1) APB and CSF faults "chemical" while the (1 0 0) APB and SISF faults "structural". The simulation results shown in Fig. 3 are consistent with this classification.

## 6. Point defects and diffusion in $Ni_3Al$

Point defects accommodate off-stoichiometry and mediate atomic diffusion in intermetallic compounds. To calculate their formation free energies and equilibrium concentrations in $Ni_3Al$, we will follow the scheme proposed in [60]. Neglecting interstitials, $Ni_3Al$ supports four types of point defect: vacancies $V_{Ni}$ and $V_{Al}$ and antisites $Al_{Ni}$ and $Ni_{Al}$ (the subscript refers to the sublattice). So-called "raw" formation energies, entropies and volumes of individual point defects have been computed using a 864-atom cubic supercell. A single point defect was created in the center of the supercell and the total energy was minimized with respect to local atomic displacements and the supercell volume. The raw defect energy $\varepsilon_P$ ($P = V_{Ni}$, $V_{Al}$, $Al_{Ni}$ or $Ni_{Al}$) is defined as the energy difference between the defected supercell and the initial perfect one. Likewise, the raw defect entropy $s_P$ is the entropy difference between the defected and perfect supercells. The entropy is identified with the vibrational entropy and the latter is treated within the classical harmonic approximation [61]. This calculation requires a construction and diagonalization of the dynamical matrix of the supercell, followed by a substitution of the obtained normal vibrational frequencies in the standard expression for the harmonic entropy. One corner atom of the supercell is fixed (excluded from the dynamical matrix) to eliminate the three translational degrees of freedom. The raw formation volume $\Omega_P$ is defined as the volume change during the supercell relaxation.

The raw formation energies, entropies and volumes calculated with the present EAM potential are listed in Table 9. The raw vacancy volumes are negative as expected. The $Ni_{Al}$ antisite volume is also negative due to the smaller atomic size of Ni relative to Al. For the same reason, the $Al_{Ni}$ antisite volume is positive. The atomic size difference is also responsible for the different signs of the antisite entropies. Indeed, the lattice around an $Al_{Ni}$ antisite is compressed. This compression gives rise to high-frequency modes in the vibrational spectrum and thus a reduction in the vibrational entropy. In contrast, lattice regions around a $Ni_{Al}$ antisite are under tension and the vibrational spectrum is slightly shifted towards low frequencies, resulting in a larger entropy.

Table 9
Calculated raw formation energies ($\varepsilon_P$), entropies ($s_P$), and volumes ($\Omega_P$) of point defects in $Ni_3Al$

| Defect | $\varepsilon_P$ (eV) | $s_P/k_B$ | $\Omega_P/\Omega_0$ |
|---|---|---|---|
| $V_{Ni}$ | 6.262 | −4.957 | −0.144 |
| $V_{Al}$ | 6.428 | −3.727 | −0.240 |
| $Al_{Ni}$ | 0.893 | −0.486 | 0.273 |
| $Ni_{Al}$ | 0.781 | 1.141 | −0.213 |

The entropies were calculated within the harmonic approximation to atomic vibrations.

Raw properties of an individual point defect are not sufficient for calculating its equilibrium concentration. This is because point defects can convert to each other through various defect reactions. For example, an Al vacancy exchanging with a neighboring Ni atom creates a $Ni_{Al}$ antisite and becomes an Ni vacancy. Under equilibrium conditions, point defects appear in such amounts that to satisfy dynamic equilibrium with respect to all possible reactions and at the same time preserve the initial (generally, non-stoichiometric) chemical composition of the compound. The calculation of equilibrium defect concentrations is, therefore, a global problem that involves raw properties of all defects. Such calculations are usually based on the lattice gas model of non-interacting point defects [60,62–64]. The input data for the model are the raw free energies of individual defects, $g_P = \varepsilon_P - Ts_P + p\Omega_P$ ($p$ being the external pressure), as well as the perfect lattice free energy $g_0 = E_0 - Ts_0 + p\Omega_0$, where $s_0 = 6.383k_B$/atom is the perfect lattice entropy. Equations expressing thermodynamic equilibrium conditions are solved for defect concentrations numerically using the iterative procedure described in [60]. In this work, all calculations are performed at zero pressure.

The calculated equilibrium defect concentrations (number per lattice site) as functions of the chemical composition at $T = 1000$ K are presented in Fig. 4. This plot shows that deviations from the stoichiometry are accommodated predominantly by antisite defects, whereas the vacancy concentrations remain relatively low. In Ni-rich compositions, the excess Ni atoms reside predominantly on the Al sublattice as $Ni_{Al}$ antisites. Likewise, in Al-rich compositions the excess Al atoms reside on the Al sublattice as $Al_{Ni}$ antisites.

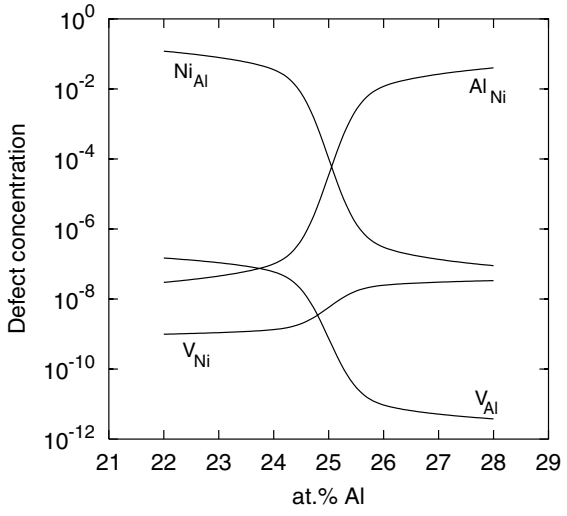


Fig. 4. Equilibrium point defect concentrations in $Ni_3Al$ as functions of chemical composition at 1000 K. Calculated with the present EAM potential using the lattice gas model of non-interacting defects. The point-defect entropy is included in the harmonic approximation.

Even in stoichiometric $Ni_3Al$, in which all point defects represent thermal excitations, the antisite concentrations are about four orders of magnitude higher than vacancy concentrations. This behavior is observed at all temperatures up to the melting point and is consistent with experimental positron annihilation measurements [65].

We will now describe a crude but very useful analytical model of point defects in $Ni_3Al$. As a first approximation, we can neglect the existence of vacancies and consider $Ni_3Al$ as a lattice gas of non-interacting antisites. Then, the model equations are solved analytically to give the following expressions for the atomic fractions of antisites relative to their sublattices [60]:

$$X_{Al_{Ni}} = -\frac{x}{2a} + \left(\frac{x^2}{4a^2} + \frac{b}{a}K\right)^{1/2}, \tag{13}$$

$$X_{Ni_{Al}} = \frac{x}{2b} + \left(\frac{x^2}{4b^2} + \frac{a}{b}K\right)^{1/2}, \tag{14}$$

where

$$K = \exp\left(-\frac{g_{Al_{Ni}} + g_{Ni_{Al}}}{k_B T}\right). \tag{15}$$

To keep these equations more general we represent the compound in the form $Ni_{a+x}Al_{b-x}$, where $a + b = 1$ and the off-stoichiometry $x$ is related to the Al composition (atomic fraction) $c_{Al}$ by

$$c_{Al} = b - x. \tag{16}$$

For $Ni_3Al$, $a = 3/4$ and $b = 1/4$. Knowing the antisite concentrations, we can find the vacancy concentrations from the conditions of dynamic equilibrium with respect to defect reactions involving both vacancies and antisites. This gives us [60]

$$X_{V_{Ni}} = \left(X_{Al_{Ni}}\right)^b \exp\left(-\frac{g_{V_{Ni}} + g_0 - bg_{Al_{Ni}}}{k_B T}\right), \tag{17}$$

$$X_{V_{Al}} = \left(X_{Ni_{Al}}\right)^a \exp\left(-\frac{g_{V_{Al}} + g_0 - ag_{Ni_{Al}}}{k_B T}\right). \tag{18}$$

In the particular case of a stoichiometric composition ($x = 0$), Eqs. (13)–(15) reduce to the following exponential expressions:

$$X_{Al_{Ni}} = \left(\frac{b}{a}\right)^{1/2} \exp\left(-\frac{g_{Al_{Ni}} + g_{Ni_{Al}}}{2k_B T}\right), \tag{19}$$

$$X_{Ni_{Al}} = \left(\frac{a}{b}\right)^{1/2} \exp\left(-\frac{g_{Al_{Ni}} + g_{Ni_{Al}}}{2k_B T}\right). \tag{20}$$

Given that the raw free energies are linear functions of temperature, Eqs. (19) and (20) reproduce the Arrhenius law. Combining them with Eqs. (17) and (18), the vacancy concentrations also depend on temperature through Arrhenius exponents. Furthermore, it turns out that defect concentrations in Ni-rich and Al-rich com-

Table 10
Effective formation energies of point defects in stoichiometric, Ni-rich and Al-rich $Ni_3Al$ calculated with the present EAM potential and by first-principles methods

| | Al-rich | Stoichiometric | N-rich |
|---|---|---|---|
| $V_{Ni}$: | | | |
| Expression | $\varepsilon_{V_{Ni}} + E_0 - b\varepsilon_{Al_{Ni}}$ | $\varepsilon_{V_{Ni}} + E_0 + \frac{b}{2}(\varepsilon_{Ni_{Al}} - \varepsilon_{Al_{Ni}})$ | $\varepsilon_{V_{Ni}} + E_0 + b\varepsilon_{Ni_{Al}}$ |
| EAM | 1.419 | 1.628 | 1.837 |
| Ab initio[a] | 1.683 | 1.863 | 2.043 |
| $V_{Al}$: | | | |
| Expression | $\varepsilon_{V_{Al}} + E_0 + a\varepsilon_{Al_{Ni}}$ | $\varepsilon_{V_{Al}} + E_0 - \frac{a}{2}(\varepsilon_{Ni_{Al}} - \varepsilon_{Al_{Ni}})$ | $\varepsilon_{V_{Al}} + E_0 - a\varepsilon_{Ni_{Al}}$ |
| EAM | 2.478 | 1.850 | 1.222 |
| Ab initio[a] | 3.213 | 2.673 | 2.133 |
| $Al_{Ni}$: | | | |
| Expression | 0 | $\frac{1}{2}(\varepsilon_{Al_{Ni}} + \varepsilon_{Ni_{Al}})$ | $\varepsilon_{Al_{Ni}} + \varepsilon_{Ni_{Al}}$ |
| EAM | 0 | 0.837 | 1.674 |
| Ab initio[a] | 0 | 0.720 | 1.440 |
| $Ni_{Al}$: | | | |
| Expression | $\varepsilon_{Al_{Ni}} + \varepsilon_{Ni_{Al}}$ | $\frac{1}{2}(\varepsilon_{Al_{Ni}} + \varepsilon_{Ni_{Al}})$ | 0 |
| EAM | 1.674 | 0.837 | 0 |
| Ab initio[a] | 1.440 | 0.720 | 0 |

$a = 3/4$ and $b = 1/4$ are stoichiometric coefficients for $Ni_3Al$.
[a] Ref. [66].

positions also follow the Arrhenius law but with different exponents. Table 10 summarizes the energies appearing in all exponential expressions relating to different compositions and types of point defect. Those energies are called the *effective formation energies* of point defects because it is these quantities that are deduced from the slopes of experimental Arrhenius plots of defect concentrations. It should be emphasized that the off-stoichiometric expressions in Table 10 are only valid if $x$ greatly exceeds all defect concentrations. For an arbitrary composition, defect concentrations do not have to follow the Arrhenius law exactly. The effective formation entropies and volumes are given by expressions similar to those in Table 10 up to the replacements $\varepsilon_P \to s_P$, $E_0 \to s_0$ and $\varepsilon_P \to \Omega_P$, $E_0 \to \Omega_0$, respectively.

Table 10 also contains the effective formation energies obtained with the present EAM potential and by first-principles calculations [66]. The agreement between the two calculation methods is satisfactory. The EAM-predicted effective formation energy of Ni vacancies in stoichiometric $Ni_3Al$, 1.628 eV, is in excellent agreement with the experimental value, 1.6 eV [67].

Returning to Fig. 4, we observe that antisite concentrations in off-stoichiometric compositions can be as high as a few atomic per cent. Under such conditions, interactions between antisites can be a significant factor in thermodynamic properties of the compound (Section 7). Binding energies of antisites have been calculated using the same 864-atom supercell as for single defects. The binding energy is defined as the raw energy of a pair of neighboring antisites minus the sum of raw energies of isolated antisites. The binding energy of two $Al_{Ni}$ antisites was found to be 0.391 eV for first neighbors and 0.030 eV for second neighbors. $Ni_{Al}$ antisites can only be second neighbors and their binding energy is small, 0.024 eV. In all three cases the antisites repel each other. It should be pointed out, however, that these binding energies only include direct interactions between neighboring antisites. Since antisites have non-zero formation volumes, they produce long-range elastic fields and can interact also through image forces existing at the crystal surface [68]. This second component of binding, which becomes quite noticeable at large antisite concentrations, is attractive for $Ni_{Al}$ antisites (negative formation volume) and repulsive for $Al_{Ni}$ antisites (positive formation volume) [68]. In effect, the image forces tend to decrease the $Ni_{Al}$–$Ni_{Al}$ binding energy and increase the $Al_{Ni}$–$Al_{Ni}$ binding energy. A more detailed analysis of the image forces will be reported elsewhere.

Diffusion mechanisms in $Ni_3Al$ are not well understood at present. Ni is believed to diffuse along its own sublattice by the simple vacancy mechanism [11–14]. Al diffusion mechanisms are essentially unknown but are likely to be more complex than for Ni diffusion. Since Al atoms are isolated from one another in the $L1_2$ structure, the mechanism of nearest-neighbor vacancy jumps is prohibited. Molecular static calculations of vacancy jump barriers [11,13,14] suggest that Al could diffuse by either 6-jump vacancy cycles or exchanges between $Al_{Ni}$ antisites and Ni vacancies.

For the jump barrier of a Ni vacancy on the Ni sublattice, our EAM potential gives 1.242 eV in excellent agreement with the experimental value 1.2 eV [67]. By adding this barrier to the effective formation energy of Ni vacancies (Table 10), the lower bound of the activation energy $Q$ of Ni diffusion in stoichiometric $Ni_3Al$ can be obtained. This results in $Q = 1.628 + 1.242 = 2.87$ eV, while experimental radiotracer measurements

give $Q = 3.14$ eV [69]. This agreement is encouraging, especially considering that jump-correlation effects and the presence of antisites at finite temperatures are likely to retard the diffusion process and thus effectively increase the activation energy. A more detailed study of diffusion mechanisms in $Ni_3Al$ by molecular dynamics simulations with the present EAM potential is currently under way and will be published elsewhere.

## 7. Thermodynamic calculations

As a test of the ability of the present EAM potential to predict high-temperature properties of the $\gamma$ and $\gamma'$-phases, the $\gamma/\gamma'$ equilibrium lines on the Ni–Al phase diagram have been calculated. This test is important in connection with possible applications of this potential to model $\gamma'$ particle precipitation and the $\gamma/\gamma'$ structure in Ni–Al alloys. The $\gamma'/\beta$ lines of the phase diagram have also been calculated as a further test of transferability of the potential.

The first step of the calculation was to obtain Gibbs free energies, $g(T)$, of pure Ni and Al and perfectly ordered $Ni_3Al$ and NiAl. Recognizing that a phase diagram construction requires highly accurate free energies, the calculations were performed beyond the harmonic approximation. During the NPT Monte Carlo simulations applied for the calculation of thermal expansion factors in Section 4, the computer code also delivered the average potential energy of the crystal per atom, $\varepsilon(T)$, at each temperature $T$. The total energy per atom, $\varepsilon_{tot}(T)$, was then obtained by adding to $\varepsilon(T)$ the classical kinetic energy $3k_BT/2$: $\varepsilon_{tot}(T) = \varepsilon(T)+3k_BT/2$. Because we assume that $p = 0$, $\varepsilon_{tot}(T)$ can be identified with the enthalpy $h(T)$. Each $h(T)$ curve, which contained 20–30 points, was approximated by a quadratic function

$$h(T) = h_0 + AT + BT^2 \tag{21}$$

with fitting parameters $h_0$, $A$ and $B$. The free energy was then recovered by integrating the Gibbs equation [70] from a reference temperature $T^0$ to a temperature $T > T^0$:

$$g(T) = g^0\frac{T}{T^0} + h_0\left(1 - \frac{T}{T^0}\right) - BT(T - T^0) - AT\ln\left(\frac{T}{T^0}\right). \tag{22}$$

The absolute value of the reference free energy $g^0$ at $T = T^0$ was obtained in the classical quasi-harmonic approximation [71]. Notice that this approximation also mimics the $p = 0$ condition and takes into account thermal expansion, although in a more approximate manner. The same reference temperature $T^0 = 400$ K was chosen for all four materials. The thermodynamic parameters obtained are summarized in Table 11.

As a test, the quasi-harmonic approximation was applied to calculate the free energy at several temperatures above $T^0$. Fig. 5 shows a comparison of the two

Table 11
Thermodynamic parameters describing Ni, Al, $Ni_3Al$ and NiAl

| | $g^0$ (eV) | $h_0$ (eV) | $A$ ($10^{-3}$/K) | $B$ ($10^{-6}$/K$^2$) |
|---|---|---|---|---|
| Ni | −4.4833 | −4.4486 | 0.24816 | 0.021332 |
| Al | −3.3967 | −3.3585 | 0.24134 | 0.052794 |
| $Ni_3Al$ | −4.6477 | −4.6247 | 0.25443 | 0.013425 |
| NiAl | −4.5058 | −4.4945 | 0.25084 | 0.018443 |

The reference temperature is $T^0 = 400$ K.

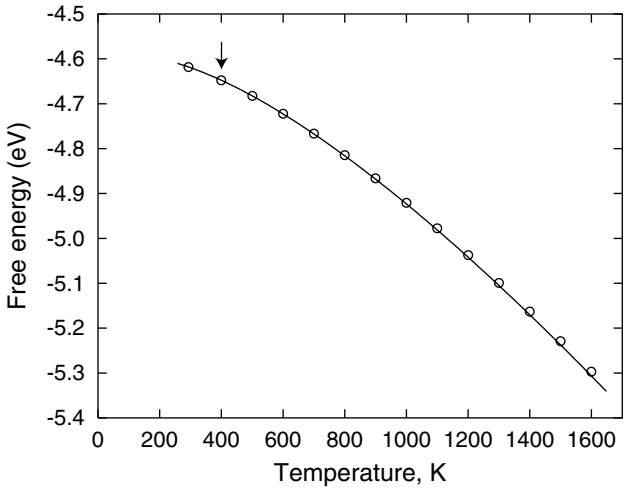


Fig. 5. Free energy of stoichiometric $Ni_3Al$ calculated in the quasi-harmonic approximation (points) and by thermodynamic integration of Monte Carlo data (line). The arrow marks the reference temperature of integration.

calculation methods for $Ni_3Al$. In agreement with previous work [71], the quasi-harmonic approximation is observed to provide fairly accurate free energies over a wide temperature range. At high temperatures, however, there is a noticeable discrepancy between the two methods. We emphasize that even such seemingly small discrepancies (on the order of 0.01 eV) are capable of having a significant impact on the phase diagram calculation.

At a next step of the calculation, grand-canonical Monte Carlo simulations were applied to compute thermodynamic properties of the $\gamma$, $\gamma'$ and $\beta$-phases. In such simulations, the total number of atoms in the simulation block is fixed while their chemical sorts are allowed to switch randomly between Ni and Al [9,72]. At a fixed temperature, the equilibrium state of the system depends on the chemical potential difference $\Delta\mu = \mu_{Al} - \mu_{Ni}$, which is kept fixed during the simulation. As trial moves, not only individual atoms are subject to random displacements but also all three dimensions of the simulation block are allowed to fluctuate to ensure a zero stress condition in each direction. The simulations employed a 864-atom supercell for the FCC lattice and a 1024-atom supercell for the BCC lattice ($\beta$-NiAl is an ordered BCC-phase). For each temperature and $\Delta\mu$, the system was equilibrated by

about $10^7$ Monte Carlo steps followed by a calculation of its equilibrium chemical composition during another $10^7$ steps. Each run was repeated for three different initial states: FCC-Ni, $Ni_3Al$ or NiAl. A plot of the equilibrium composition against $\Delta\mu$ for a fixed $T$ allows one to reconstruct an isothermal section of the phase diagram, with continuous segments of the plots representing single-phase fields and concentration jumps corresponding to two-phase regions [9].

Fig. 6 shows our simulation results for $T = 1000$ K. The plots obtained for the temperatures of 700, 1300 and 1500 K look qualitatively similar. When $\Delta\mu$ is small, the alloys always equilibrates into a disordered $\gamma$-phase regardless of the initial state. As $\Delta\mu$ increases, Al concentration in the $\gamma$-phase also increases and at $\Delta\mu \approx -0.43$ eV makes a jump from 14.8 to 23.0 at.%. In the new state the alloy has an ordered $L1_2$ structure corresponding to Ni-rich $\gamma'$-phase. Although this transition is first-order, no hysteresis was detected: both the position of the jump and the solubility limits in the phases were practically the same regardless of whether the simulations started from the ordered of disordered state. This observation suggests a very low nucleation barrier of the $\gamma/\gamma'$ transformation at all temperatures studied here.

As $\Delta\mu$ increases further, the $\gamma'$-phase becomes stoichiometric, then Al-rich, and at some point it spontaneously transforms to the $\beta$-phase by developing a tetragonal distortion with a simultaneous change in the ordering. This transformation, which crystallographically is similar to the inverse of the Bain transformation in steel, was possible because the shape of the simulation block was allowed to fluctuate. Conversely, in simulations started from the $\beta$-phase a transformation to the $\gamma'$-phase occurred by a tetragonal deformation along the Bain path. In contrast to the $\gamma/\gamma'$ transformation, the $\gamma'/\beta$ transformation is accompanied by a considerable hysteresis (Fig. 6). This is not surprising: while the $\gamma$ and $\gamma'$-phases share same lattice and only differ in long-range order, the $\gamma'$and $\beta$-phases have also different crystal lattices and are separated by a significant transformation barrier. Because of this hysteresis, a $c_{Al}$ versus $\Delta\mu$ plot alone does not allow us to find the $\gamma'/\beta$ lines on the phase diagram accurately.

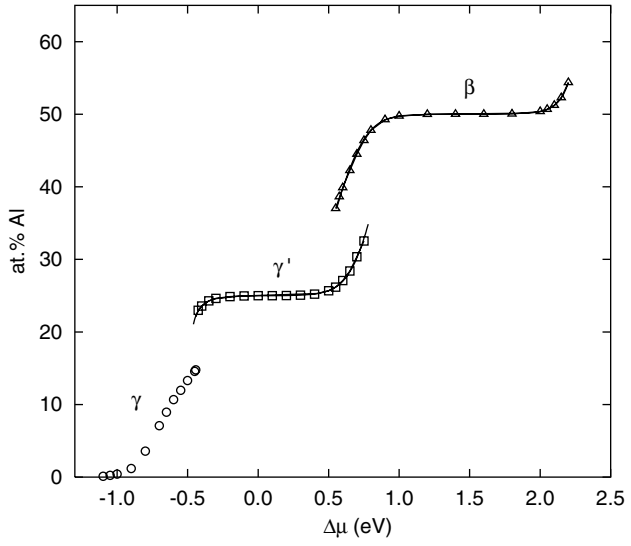


Fig. 6. Alloy composition as a function of the relative chemical potential of Ni and Al obtained by grand-canonical Monte Carlo simulations at 1000 K. (○) $\gamma$-phase, (□) $\gamma'$-phase, (△) $\beta$-phase. The curves were calculated within the thermodynamic model explained in the text.

To solve this problem, the $\Delta\mu(c_{Al}, T)$ functions of both phases were approximated by analytical expressions based a simple thermodynamics model. The model gives us the free energy functions of the phases and thus allows us to locate the phase boundaries by a common tangent construction.

We assume that off-stoichiometry of a partially ordered phase is dominated by antisites on both sublattices. By treating all configurational effects relating to antisites within the mean-field approximation, the free energy of a compound, $g_c(c_{Al}, T)$, can be expressed by

$$\begin{aligned} g_c(c_{Al}, T) = & g(T) + bX_{Ni_{Al}} g_{Ni_{Al}} + aX_{Al_{Ni}} g_{Al_{Ni}} + I_1 X_{Ni_{Al}}^2 \\ & + I_2 X_{Al_{Ni}}^2 + k_B T b X_{Ni_{Al}} \ln X_{Ni_{Al}} + k_B T a X_{Al_{Ni}} \ln X_{Al_{Ni}} \\ & + k_B T b\left(1 - X_{Ni_{Al}}\right) \ln\left(1 - X_{Ni_{Al}}\right) \\ & + k_B T a\left(1 - X_{Al_{Ni}}\right) \ln\left(1 - X_{Al_{Ni}}\right). \end{aligned} \tag{23}$$

Here $g(T)$ is the free energy of the perfectly ordered stoichiometric compound calculated previously (see Eq. (22) and Table 12). In comparison with earlier models [60,62–64], we have included two additional terms accounting for antisite–antisite interactions. These terms are quadratic in the antisite concentrations and depend on antisite interaction parameters $I_1$ and $I_2$. They are expected to come into play in Ni-rich and Al-rich compositions, respectively. Considering that antisite concentrations at stoichiometry are small (cf. Fig. 4), the cross-interaction term proportional to $X_{Ni_{Al}} X_{Al_{Ni}}$ is neglected. As a first approximation, we can plug into Eq. (23) the antisite concentrations given by Eqs. (13)–(16). This makes $g_c(c_{Al}, T)$ a closed-form expression with adjustable parameters $g_{Ni_{Al}}$, $g_{Al_{Ni}}$, $I_1$ and $I_2$.

Using Eq. (23) we have

$$\Delta\mu = -\frac{\partial g_c}{\partial x} = -\frac{\partial g_c}{\partial X_{Ni_{Al}}} \frac{\partial X_{Ni_{Al}}}{\partial x} - \frac{\partial g_c}{\partial X_{Al_{Ni}}} \frac{\partial X_{Al_{Ni}}}{\partial x}, \tag{24}$$

Table 12
Antisite formation free energies and interaction parameters in $Ni_3Al$ obtained by Monte Carlo simulations

| $T$ (K) | $g_{Ni_{Al}}$ | $g_{Al_{Ni}}$ | $I_1$ | $I_2$ |
|---|---|---|---|---|
| 700 | 0.7037 | 0.8929 | −0.0481 | 0.0736 |
| 1000 | 0.6626 | 0.9023 | −0.0469 | 0.1164 |
| 1300 | 0.6138 | 0.9041 | −0.0495 | 0.1245 |
| 1500 | 0.5751 | 0.8932 | −0.0519 | 0.2306 |

where

$$\frac{\partial g_c}{\partial X_{\mathrm{Ni_{Al}}}} = b g_{\mathrm{Ni_{Al}}} + 2I_1 X_{\mathrm{Ni_{Al}}} + k_B T b \ln \frac{X_{\mathrm{Ni_{Al}}}}{1 - X_{\mathrm{Ni_{Al}}}}, \quad (25)$$

$$\frac{\partial g_c}{\partial X_{\mathrm{Al_{Ni}}}} = a g_{\mathrm{Al_{Ni}}} + 2I_2 X_{\mathrm{Al_{Ni}}} + k_B T a \ln \frac{X_{\mathrm{Al_{Ni}}}}{1 - X_{\mathrm{Al_{Ni}}}}, \quad (26)$$

$$\frac{\partial X_{\mathrm{Ni_{Al}}}}{\partial x} = \frac{1}{2b} + \frac{x/4b^2}{(x/4b^2 + aK/b)^{1/2}}, \quad (27)$$

$$\frac{\partial X_{\mathrm{Al_{Ni}}}}{\partial x} = -\frac{1}{2a} + \frac{x/4a^2}{(x/4a^2 + bK/a)^{1/2}}. \quad (28)$$

Again, Eqs. (24)–(28) provide a closed-form expression for $\Delta\mu(c_{\mathrm{Al}}, T)$, which can be fit to the Monte Carlo $\Delta\mu(c_{\mathrm{Al}})$ curves of individual phases by adjusting the parameters $g_{\mathrm{Ni_{Al}}}$, $g_{\mathrm{Al_{Ni}}}$, $I_1$ and $I_2$. These parameters known, Eq. (23) gives us the free energy curves $g_c(c_{\mathrm{Al}})$ of the phases at a given temperature $T$. The equilibrium phase concentrations are then readily calculated by the common tangent construction implemented numerically.

This procedure was applied to the $\gamma'$ and β-phases at four temperatures. The fitting parameters obtained for the $\gamma'$-phase are listed in Table 12. Fig. 7 shows the Ni-rich half of the experimental phase diagram [73] in comparison with our calculations. The agreement with experiment is quite satisfactory. Most of the discrepancy originates from the thermodynamic part of the calculation, which is especially sensitive to the stoichiometric free energies $g(T)$. In particular, the use of the quasi-harmonic approximation for $g(T)$ instead of thermodynamic integration leads to a considerably worse agreement with experiment. The finite size of the simulation block employed in the Monte Carlo simulations could also contribute to the discrepancy. Notice that no experimental thermodynamic data were used for generating the EAM potential, except for the lattice parameters of Ni, Al and $Ni_3Al$ and the cohesive energies of Ni and Al. The reasonable agreement with the experimental phase diagram points to a good transferability of the potential to atomic configurations occurring in the γ and $\gamma'$-phases at high temperatures, as well as to its potential utility for modeling two-phase $\gamma/\gamma'$ alloys.

It should be admitted that the antisite disorder model underlying these calculations contradicts the well-established experimental fact that Al-rich compositions of the β-phase are dominated by structural vacancies on the Ni sublattice [74]. Vacancies are not included in our model. However, it is the free energy of Al-deficient compositions that determines the $\gamma'$/β-phase equilibrium. Such compositions do not contain structural vacancies and are governed by the antisite disorder mechanism. This explains why the $\gamma'$/β lines of the calculated phase diagram are also consistent with experiment.

Fig. 8 compares the antisite free energies in $Ni_3Al$, $g_{\mathrm{Ni_{Al}}}$ and $g_{\mathrm{Al_{Ni}}}$, obtained by fitting our thermodynamic model to Monte Carlo results (Table 12), on one hand, and calculated directly by molecular statics in conjunction with the harmonic approximation, on the other hand (Table 9). Although the agreement between these two essentially different calculation methods is reasonable, significant deviations are observed at high temperatures. The harmonic approximation neglects thermal expansion and other anharmonic effects, which is likely to be the main source of the discrepancy [9,75].

The positive sign of the antisite interaction parameter $I_2$ is consistent with the repulsion between $Al_{Ni}$ antisites

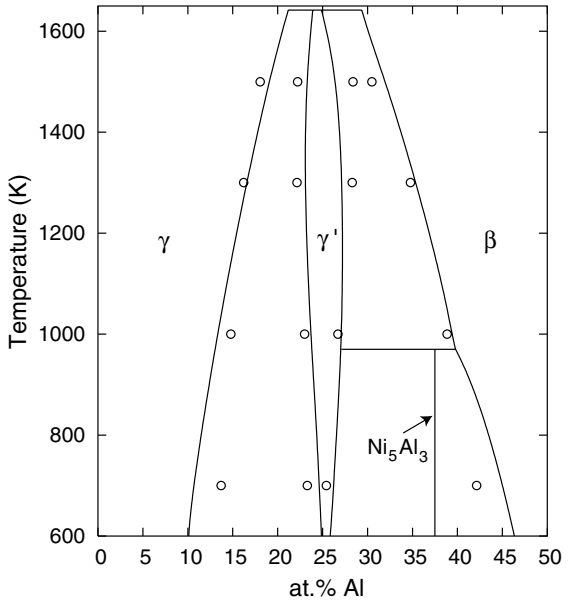


Fig. 7. Calculated (points) and experimental (lines) phase diagram of the NiAl system.

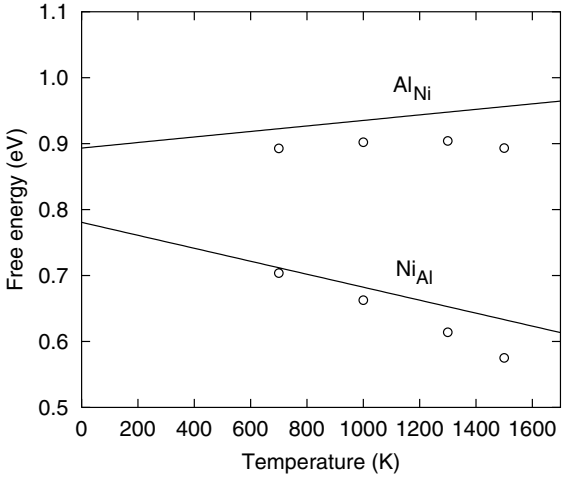


Fig. 8. Free energies of antisite formation in $Ni_3Al$ deduced from Monte Carlo simulations (points) and calculated using molecular statics and the harmonic approximation (lines).

predicted in Section 6 by static calculations. Those calculations also predicted the $Ni_{Al}$–$Ni_{Al}$ interaction to be repulsive and very weak. The respective interaction parameter, $I_1$, came out to be also small but negative (slight attraction). One source of this discrepancy can be the entropy effect that was neglected in Section 6. In addition, those calculations neglected the image forces that, at high antisite concentrations, should favor an attraction between $Ni_{Al}$ antisites.

## 8. Coherent Ni/$Ni_3Al$ interfaces

Using the new potential, the energies of coherent Ni/$Ni_3Al$ interfaces, which can be considered as a simple prototype of $\gamma/\gamma'$ interfaces, have been calculated for three different interface orientations. To this end, a rectangular supercell was created with desired crystal planes parallel to one of its faces. A plane dividing the supercell in two equal halves was chosen as an interface. In the planes lying on one side of the interface, all Al atoms were replaced by Ni, thus effectively creating a multi-layered structure containing equal amounts of the Ni an $Ni_3Al$-phases. The supercell was relaxed statically by allowing both local atomic displacements and size variations in all three directions. The apparent interface energy $\alpha$ was determined from the relation

$$\alpha = \frac{E(2N) - NE_0(\mathrm{Ni}) - NE_0(\mathrm{Ni_3Al})}{2S}. \tag{29}$$

Here $E(2N)$ is the relaxed energy of the simulation block containing $2N$ atoms, $E_0(\mathrm{Ni})$ and $E_0(\mathrm{Ni_3Al})$ are cohesive energies of FCC Ni and $Ni_3Al$, respectively, and $S$ is the cross-sectional area of the block parallel to the interface.

Since the interface is fully coherent, both phases are elastically strained due to the 1.44% lattice parameter mismatch existing between Ni and $Ni_3Al$. The equilibrium value of the common lattice parameter of the phases is close but not identical to the average between the two phases because their elastic constants are different. The elastic strain energy of the phases contributes to $E(2N)$ and leads to overestimated $\alpha$ values delivered by Eq. (29). To eliminate the strain energy contribution, we can take advantage of the fact that it is proportional to the volumes of the phases [76]. Since our simulation block contains equal amounts of the phases and $S$ is kept fixed, the strain energy is proportional to the supercell size $L$ in the direction normal to the interface. Therefore, the true interface energy can be recovered by calculating $\alpha$ for several supercell sizes and extrapolating the results to $L \to 0$ [76,77].

Such calculations were implemented for the interface orientations (1 0 0), (1 1 0) and (1 1 1). The apparent $\alpha$ values were found to follow a linear correlation with $L$ very accurately (Fig. 9) and the $L \to 0$ extrapolation gave the following interface energies: $\alpha_{(100)} = 46$ mJ/m$^2$, $\alpha_{(110)} = 28$ mJ/m$^2$ and $\alpha_{(111)} = 12$ mJ/m$^2$. These numbers appear very reasonable. For comparison, first-principles calculations by Price and Cooper [78] gave $\alpha_{(100)} = 63$ or 25 mJ/m$^2$ depending on the magnetic states of the phases. Experimental interface energies determined from $\gamma'$ coarsening kinetics in $\gamma/\gamma'$ alloys vary between 8 and 20 mJ/m$^2$, see for example [79]. In coarsening experiments, the $\gamma'$ particles are either spherical (for small sizes) or have a cuboidal shape with (1 0 0) faces dictated by the elastic anisotropy of the matrix. Hence, it is either $\alpha_{(100)}$ or an average over different orientations that should be compared with experiment.

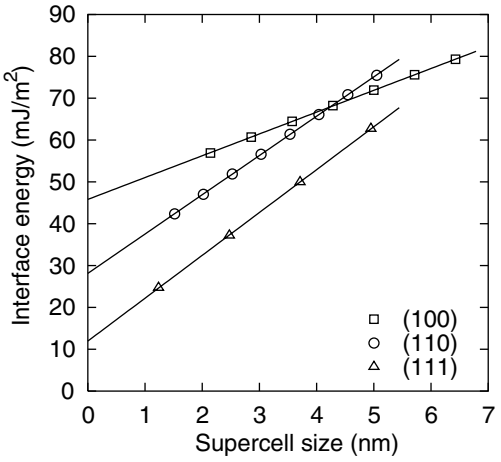


Fig. 9. Apparent energies of coherent Ni/$Ni_3Al$ interfaces with three different orientations as functions of the supercell size. The true interface energy is obtained by extrapolation to zero supercell size.

That both first-principles and our EAM calculations give interface energies lying on the higher side of the experiment is understandable. In $\gamma/\gamma'$ alloys, the concentration jump across the interface is smaller than for ideal Ni/$Ni_3Al$ interfaces. In addition, the long-range order parameter does not change across a $\gamma/\gamma'$ interface as abruptly as it does across a Ni/$Ni_3Al$ interface. Both factors should lead to lower energies of $\gamma/\gamma'$ interfaces. The entropy may also contribute to the experimental interface free energies, which are measured at high temperatures.

Fig. 10 illustrates some of these effects by plotting the Al concentration, averaged over individual (2 0 0) atomic layers, as a function of distance across the (1 0 0)$\gamma/\gamma'$ interface at 700 K. These results were obtained by grand canonical Monte Carlo simulations (Section 7) on a 1536-atom supercell containing a coherent (1 0 0)$\gamma/\gamma'$ interface. The relative chemical potential of Ni and Al was adjusted so that to prevent the interlace migration, that is to ensure coherent two-phase equilibrium in the system. The amplitude of concentration oscillations on the $\gamma'$ side characterizes the long-range order in this phase. Notice that the long range order does not drop to zero abruptly at the interface

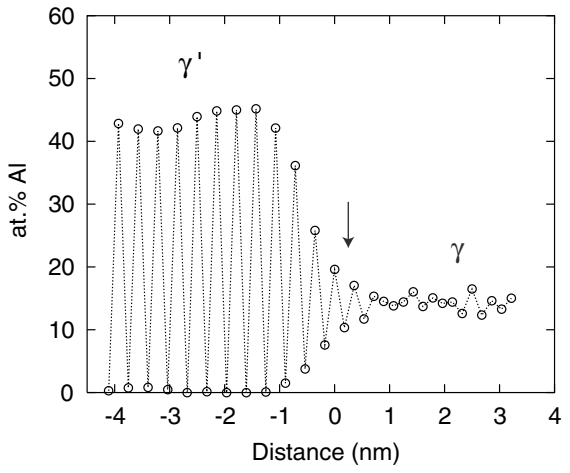


Fig. 10. Concentration profile across the coherent (1 0 0)$\gamma/\gamma'$ interface obtained by grand-canonical Monte Carlo simulations at 700 K. The points represent Al concentration in individual (2 0 0) layers parallel to the interface. The arrow marks the initial position of the interface at 0 K.

plane but rather decays gradually over 4–6 (2 0 0) layers around the interface, as does also the average Al concentration. The Al concentration jump across the interface is about 8 at.% and not 25 at.% as for a Ni/$Ni_3Al$ interface. Notice also that the off-stoichiometry of the $\gamma'$-phase occurs by a depletion of the Al sublattice in Al, while Al concentration on the Ni sublattice remains extremely small. This behavior is well consistent with the antisite concentrations calculated in Section 6 (cf. Fig. 4).

## 9. Discussion and conclusions

The EAM potential developed in this work provides an accurate description of a spectrum of properties of Ni, Al and $Ni_3Al$, including elastic constants, thermal expansion, point defects and planar faults. Furthermore, properties of the $\gamma$ and $\gamma'$-phases formed by Ni and $Ni_3Al$ at elevated temperatures are also represented accurately. In particular, their phase fields on the Ni–Al phase diagram are reproduced in a reasonable agreement with experiment. It has been demonstrated that the potential is suitable for the modeling of $\gamma/\gamma'$ interphase boundaries.

It is interesting to examine how well other phases of the Ni–Al system are represented by the potential. When developing the potential, we did not use any experimental data for B2–NiAl, although first-principles energy-volume curves for six compounds with this stoichiometry were included in the fitting database. The fact that the $\gamma'/\beta$ lines of the calculated phase diagram are consistent with experiment (Fig. 7) gives an indication that the potential works for NiAl reasonably well. Indeed, calculations show that the potential accurately reproduces the experimental lattice parameter and cohesive energy of NiAl (Table 13) and gives reasonable

Table 13
Lattice properties of NiAl calculated with the present EAM potential in comparison with experimental data

| | $a_0$ (nm) | $E_0$ (eV) | Elastic constants (GPa) | | |
|---|---|---|---|---|---|
| | | | $c_{11}$ | $c_{12}$ | $c_{44}$ |
| Experiment | 0.288[a] | −4.50[b] | 199[c] | 137[c] | 116[c] |
| EAM | 0.2862 | −4.4974 | 297 | 206 | 171 |

None of these properties were included in the fitting database.
[a] Ref. [31].
[b] Ref. [85].
[c] Ref. [86].

thermal expansion factors (Fig. 2(c)). The (1 1 0) APB energy, 591 mJ/m$^2$, compares well with both experimental (>500 mJ/m$^2$ [80]) and first-principles data (880 mJ/m$^2$ [81]; 810 mJ/m$^2$ [82]). The agreement with first-principles formation energies of alternate structures of NiAl is also good (Table 7). However, the elastic constants are almost 50% higher than their experimental counterparts (Table 13). Furthermore, the so-called interbranch Al energy of point defects in NiAl [24,62–64] is negative, meaning that the existence of Ni structural vacancies in Al-rich compositions is energetically unfavorable. This contradicts to both experimental data [74] and first-principles calculations [63,64].

This lack of good transferability to NiAl is a common problem of other potentials fit to $Ni_3Al$ properties. For example, elastic constants of NiAl calculated with the VC potential [18] are also about 50% off the experiment values and the interbranch Al energy is negative. In addition, the $L1_0$ structure of NiAl is incorrectly predicted to be more stable than B2. On the other hand, potentials fit directly to NiAl properties [24,83], while describing such properties accurately, do not perform well for $Ni_3Al$. For instance, the potential of Ludwig and Gumbsch [83] constructed for NiAl predicts the $D0_{19}$ structure of $Ni_3Al$ to be more stable than the correct $L1_2$ structure.

Regarding other compounds of this system, the present potential predicts the $L1_2$ structure of $NiAl_3$ to be more stable than $D0_{11}$, which is incorrect. Our previous NiAl potential [24] correctly predicts the experimentally observed $D0_{11}$ structure of $NiAl_3$ to be the ground state but its formation energy is practically identical to the average formation energy of NiAl and Al, meaning that $NiAl_3$ should not appear on the phase diagram. Experimentally, this compound exists on the phase diagram below 1127 K. With the present potential as well as the one of [24], the experimentally observed $Ni_5Al_3$ compound is unstable: its formation energy lies above the average formation energy of $Ni_3Al$ and NiAl. It is not surprising, therefore, that this compound was not found in our Monte Carlo simulations (Section 7). Likewise, both potentials predict the $Ni_3Al_4$ and $Ni_2Al_3$ compounds to be unstable against decomposition into NiAl and Al.

Overall, none of the EAM potentials that we have tested so far gives the convex-hull plot of the ground-state formation energy versus composition in agreement with the experimental Ni–Al phase diagram. It should be mentioned that attempts to fit to the right convex hull plot were made during the construction of the NiAl potential in [24]. However, such attempts ran into conflict with the requirement of having a positive interbranch Al energy so that to stabilize constitutional vacancies in Al-rich NiAl. To make the potential applicable to diffusion simulations in NiAl [84], a positive interbranch Al energy was enforced at the expense of the correct relative stability of other phases. The likely cause of this conflict is the sensitivity of point-defect energies in NiAl to angular-dependent atomic interactions that are not captured by EAM. If this is so, an incorporation of angular terms in future interatomic potentials should allow us to reconcile a positive interbranch Al energy in NiAl with global transferability of the potential across the phase diagram.

In the meantime, existing EAM potentials should simply be applied to compounds where they work best. On the optimistic side, many of the discrepancies regarding the phase stability are actually quite small, often on the order of 0.01–0.05 eV. In many atomistic simulations such small energy differences are unlikely to affect the final results. In particular, we believe that the EAM potential proposed in this paper can be safely applied to model atomic diffusion and dislocations in $Ni_3Al$, interaction of dislocations with $\gamma/\gamma'$ interfaces, and related processes. Semi-coherent $\gamma/\gamma'$ interfaces and their effect on the dislocation motion is another appealing topic of future research.

## Acknowledgements

I am grateful to P.M. Hazzledine for helpful discussions and to M.J. Mehl and D.A. Papaconstantopoulos for making their LAPW calculation results available for this work. This work was supported by the US Air Force Office of Scientific Research (Metallic Materials Program) under Grant No. F49620-01-1-0025.

## References

[1] Pope DP. In: Cahn RW, Haasen P, editors. Physical metallurgy, vol. 3. Amsterdam: Elsevier/North-Holland; 1996. p. 207 [chapter 24].
[2] Sims CT, Stoloff NS, Hagel WC, editors. Superalloys II – high-temperature materials for aerospace and industrial applications. New York: Wiley; 1987.
[3] Pollock TM, Kissinger RD, Bowman RR, Green KA, McLean M, Olson SL, et al., editors. Superalloys 2000. Warrendale, PA: TMS; 2000.
[4] Yoo MH, Daw MS, Baskes MI. In: Vitek V, Srolovitz DJ, editors. Atomistic simulation of materials: beyond pair potentials. New York: Plenum Press; 1989. p. 401.
[5] Pasianot R, Farkas D, Savino EJ. J Phys III 1991;1:997.
[6] Vitek V, Ackland GJ, Cserti J. In: Giamei P, PopeAlloy DP, editors. Phase stability and design, vol. 186. MRS Symp. Proc. 1991. p. 237–51.
[7] Vitek V, Pope DP, Bassani JL. In: Nabarro FRN, Duesbery MS, editors. Dislocations in solids, vol. 10. Amsterdam: Elsevier/North-Holland; 1996. p. 136 [chapter 51].
[8] Wen M, Li S. Acta Mater 1998;46:4351.
[9] Foiles SM, Daw MS. J Mater Res 1987;2:5.
[10] Xie ZY, Farkas D. J Mater Res 1994;9:875.
[11] Debiaggi SB, Decorte PM, Monti AM. Phys Status Solidi (b) 1996;195:37.
[12] Herzig Chr, Divinski SV, Frank S, Przeorski T. Defect Diff Forum 2001;194–199:317.
[13] Duan J, Osetsky YN, Bacon DJ. Defect Diff Forum 2001;194–199:423.
[14] Oramus P, Kozubski R, Pierron-Bohnes V, Cadeville MC, Massobrio C, Pfeiler W. Defect Diff Forum 2001;194–199:453.
[15] Finnis MW, Sinclair JE. Philos Mag A 1984;50:45.
[16] Daw MS, Baskes MI. Phys Rev B 1984;29:6443.
[17] Baskes MI. Acta Metall Sini 1995;8:287.
[18] Voter AF, Chen SP. MRS Symp Proc 1987;82:175.
[19] Ercolessi F, Adams JB. Europhys Lett 1994;26:583.
[20] Mishin Y, Farkas D, Mehl MJ, Papaconstantopoulos DA. Phys Rev B 1999;59:3393.
[21] Landa A, Wynblatt P, Siegel DJ, Adams JB, Mryasov ON, Liu XY. Acta Mater 2000;48:1753.
[22] Baskes MI, Asta M, Srinivasan SG. Philos Mag A 2001;81:991.
[23] Mishin Y, Mehl MJ, Papaconstantopoulos DA, Voter AF, Kress JD. Phys Rev B 2001;63:224106.
[24] Mishin Y, Mehl MJ, Papaconstantopoulos DA. Phys Rev B 2002;65:224114.
[25] Li Y, Siegel DJ, Adams JB, Liu XY. Phys Rev B 2003;67:125101.
[26] Zope RR, Mishin Y. Phys Rev B 2003;68:024102.
[27] Rose JH, Smith JR, Guinea F, Ferrante J. Phys Rev B 1984;29:2963.
[28] Singh DJ. Planewaves, pseudopotentials and the LAPW method. Boston, MA: Kluwer Academic Publishers; 1994.
[29] Kohn W, Sham LJ. Phys Rev 1965;140:A1133.
[30] Johnson RA. Phys Rev B 1989;39:12554.
[31] Kittel C. Introduction to solid state physics. New York: Wiley-Interscience; 1986.
[32] Weast RC, editor. Handbook of chemistry and physics. Boca Raton, FL: CRC; 1984.
[33] Simmons G, Wang H. Single crystal elastic constants and calculated aggregate properties. Cambridge, MA: MIT Press; 1977.
[34] Metals: phonon states, electron states, and Fermi surfaces. Landolt-Bornstein, New Series, Group III, vol. 13. Berlin: Springer; 1981 [Part a].
[35] Foiles SM. Phys Rev B 1985;32:7685.
[36] Frenkel D, Smit B. Understanding molecular simulation. San Diego: Academic Press; 2002.
[37] Touloukian YS, Kirby RK, Taylor RE, Desai PD, editors. Thermal expansion: metallic elements and alloys, vol. 12. New York: Plenum Press; 1975.
[38] Schaefer H-E, Gugelmeier R, Schmolz M, Seeger A. Mater Sci Forum 1987;15–18:111.
[39] Wycisk W, Feller-Kniepmeier M. J Nucl Mater 1978;69–70:616.
[40] Balluffi RW. J Nucl Mater 1978;69–70:240.
[41] Murr LE. Interfacial phenomena in metals and alloys. Reading, MA: Addison-Wesley; 1975.
[42] Sun Y, Kaxiras E. Philos Mag A 1997;75:1117.
[43] Lu G, Kioussis N, Bulatov VV, Kaxiras E. Phys Rev B 2000;62:3099.
[44] Yoo MH. Acta Metall 1987;35:1559.

[45] Stassis C, Kayser FX, Loong CK, Arch D. Phys Rev B 1981;24:3048.
[46] Kayser FX, Stassis C. Phys Status Solidi (a) 1981;64:335.
[47] Veyssiere P, Saada G. In: Nabarro FRN, Duesbery MS, editors. Dislocations in solids, vol. 10. Amsterdam: Elsevier/North-Holland; 1996. p. 253 [chapter 53].
[48] Sun YQ, Hazzledine PM. In: Nabarro FRN, Duesbery MS, editors. Dislocations in solids, vol. 10. Amsterdam: Elsevier/North-Holland; 1996. p. 253 [chapter 49].
[49] Yoo MH. Scripta Metall 1986;20:915.
[50] Vitek V. Crystal Lattice Defects 1974;5:1.
[51] Paxton A, Sun YG. Philos Mag A 1998;78:85.
[52] Mryasov ON, Gornostyrev YN, van Schilfgaarde M, Freeman AJ. Acta Mater 2002;50:4545.
[53] Hemker K, Mills MJ. Philos Mag A 1993;68:305.
[54] Karnthaler HP, Muhlbacher ET, Rentenberger C. Acta Mater 1996;44:547.
[55] Kruml T, Conforto E, Piccolo BL, Caillard D, Martin JL. Acta Mater 2002;50:5091.
[56] Schoeck G, Kohlhammer S, Fahnle M. Philos Mag Lett 1999;79:849.
[57] Kohlhammer S, Fahnle M, Schoeck G. Scripta Mater 1998;39:359.
[58] Chen SP, Srolovitz DJ, Voter AF. J Mater Res 1989;4:62.
[59] Skinner AJ, Lill JV, Broughton JQ. Model Simul Mater Sci Eng 1995;3:359.
[60] Mishin Y, Herzig C. Acta Mater 2000;48:589.
[61] Wallace DC. Thermodynamics of crystals. New York: Wiley; 1972.
[62] Hagen M, Finnis MW. Philos Mag A 1998;77:447.
[63] Meyer B, Fähnle M. Phys Rev B 1999;59:6072.
[64] Korzhavyi PA, Ruban AV, Lozovoi AY, Vekilov YK, Abrikosov IA, Johansson B. Phys Rev B 2000;61:6003.
[65] Sun J, Lin TL. Acta Metall Mater 1994;42:195.
[66] Fu CL, Painter GS. Acta Mater 1997;45:481.
[67] Wang T, Shimotomai M, Doyama M. J Phys F 1984;14:37.
[68] Eshelby JD. In: Smallman RE, Harris JE, editors. Point defect behaviour and diffusional processes. The Metals Society; 1976. p. 3–10.
[69] Frank S, Sodervall U, Herzig Chr. Phys Status Solidi (b) 1995;191:45.
[70] Guggenheim EA. Thermodynamics. An advanced treatment for chemistis and physicists. 4th ed. Amsterdam: Elsevier/North-Holland; 1993.
[71] Foiles SM. Phys Rev B 1994;49:14930.
[72] Foiles SM. In: Dowben P, Miller A, editors. Surface segregation phenomena. CRC Press; 1990. p. 79.
[73] Massalski TB, editor. Binary alloy phase diagrams. Materials Park, OH: ASM; 1986.
[74] Bradley AJ, Taylor A. Proc Roy Soc A 1937;159:56.
[75] Rickman JM, LeSar R. Annu Rev Mater Res 2002;32:195.
[76] Benedek R, Seidman DN, Woodward C. J Phys: Condens Matter 2002;14:2877.
[77] Farkas D, de Campos MF, de Souza RM, Goldenstein H. Scripta Metall Mater 1994;30:367.
[78] Price DL, Cooper BR. Mater Res Soc Symp Proc 1996;408:463.
[79] Ardell AJ. Interface Science 1995;3:119.
[80] Veyssiere P, Noebe R. Philos Mag A 1992;65:1.
[81] Hong T, Freeman AJ. Phys Rev B 1991;43:6446.
[82] Fuand CL, Yoo MH. Acta Metall Mater 1992;40:703.
[83] Ludwig M, Gumbsch P. Model Simul Mater Sci Eng 1995;3:533.
[84] Mishin Y, Lozovoi AY, Alavi A. Phys Rev B 2003;67:014201.
[85] Hultgren R, Desai PD, Hawkins DT, Gleiser M, Kelley KK, editors. Selected values of the thermodynamics properties of binary alloys. Metals Park, OH: ASM; 1973.
[86] Rusovic N, Warlimont H. Phys Status Solidi A 1977;44:609.